WILEY
Publishers Since 1807

111 River Street, Hoboken, NJ 07030

*****IMMEDIATE RESPONSE REQUIRED*****

Your article will be published online via Wiley's EarlyView® service (www.interscience.wiley.com) shortly after receipt of corrections. EarlyView®is Wiley's online publication of individual articles in full text HTML and/or pdf format before release of the compiled print issue of the journal. Articles posted online in EarlyView® are peer-reviewed, copyedited, author corrected, and fully citable via the article DOI (for further information, visit www.doi.org). EarlyView® means you benefit from the best of two worlds—fast online availability as well as traditional, issue based archiving.

Please follow these instructions to avoid delay of publication.

READ PROOFS CAREFULLY

- This will be your only chance to review these proofs. **Please note that once your corrected article is posted online, it is considered legally published, and cannot be removed from the Web site for further corrections.**
- Please note that the volume and page numbers shown on the proofs are for position only.

ANSWER ALL QUERIES ON PROOFS (Queries for you to answer are attached as the last page of your proof.)

- Mark all corrections directly on the proofs. Note that excessive alterations may ultimately result in delay of publication and extra costs may be charged to you.

CHECK FIGURES AND TABLES CAREFULLY

- Check size, numbering, and orientation of figures.
- All images in the PDF are downsampled (reduced to lower resolution and file size) to facilitate Internet delivery. These images will appear at a higher resolution and sharpness in the printed article.
- Review figure legends to ensure that they are complete.
- Check all tables. Review layout, title, and footnotes.

RETURN **PROOFS**
CTA (If you have not already signed one)

RETURN IMMEDIATELY AS YOUR ARTICLE WILL BE POSTED ONLINE SHORTLY AFTER RECEIPT.
E-MAIL TO: MRM@wiley.com

QUESTIONS? **MRM Production Team**
E-mail: MRM@wiley.com

Refer to journal acronym and article production number (i.e., MRM 00-00000).

WILEY

USING e-ANNOTATION TOOLS FOR ELECTRONIC PROOF CORRECTION

Required software to e-Annotate PDFs: Adobe Acrobat Professional or Adobe Reader (version 11 or above). (Note that this document uses screenshots from Adobe Reader DC.)
The latest version of Acrobat Reader can be downloaded for free at: http://get.adobe.com/reader/

Once you have Acrobat Reader open on your computer, click on the Comment tab (right-hand panel or under the Tools menu).

This will open up a ribbon panel at the top of the document. Using a tool will place a comment in the right-hand panel. The tools you will use for annotating your proof are shown below:

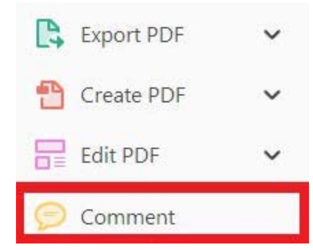

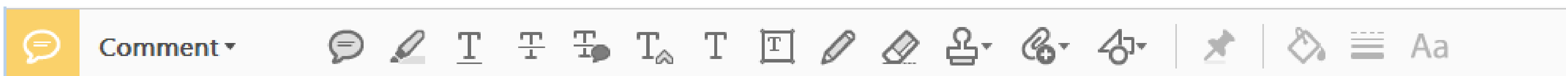

1. Replace (Ins) Tool – for replacing text.

Strikes a line through text and opens up a text box where replacement text can be entered.

How to use it:

- Highlight a word or sentence.
- Click on .
- Type the replacement text into the blue box that appears.

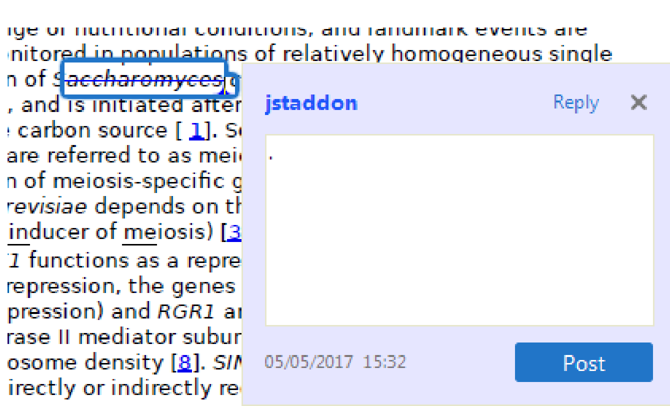

2. Strikethrough (Del) Tool – for deleting text.

Strikes a red line through text that is to be deleted.

How to use it:

- Highlight a word or sentence.
- Click on ..
- The text will be struck out in red.

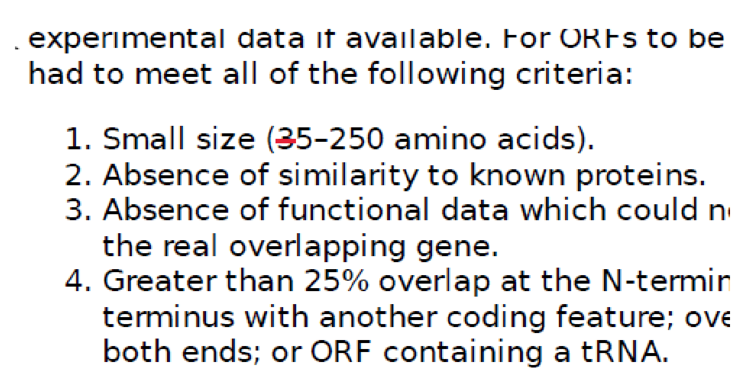

3. Commenting Tool – for highlighting a section to be changed to bold or italic or for general comments.

Use these 2 tools to highlight the text where a comment is then made.

How to use it:

- Click on .
- Click and drag over the text you need to highlight for the comment you will add.
- Click on .
- Click close to the text you just highlighted.
- Type any instructions regarding the text to be altered into the box that appears.

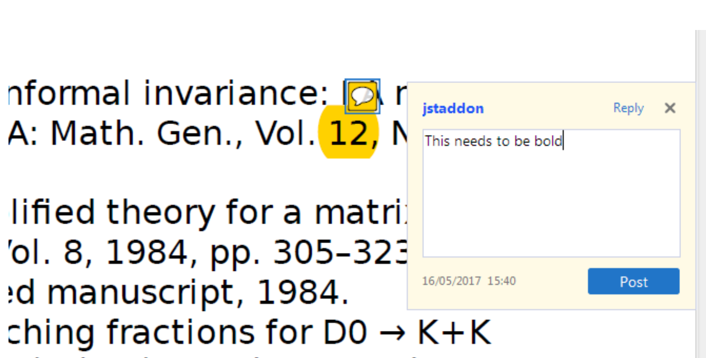

4. Insert Tool – for inserting missing text at specific points in the text.

Marks an insertion point in the text and opens up a text box where comments can be entered.

How to use it:

- Click on .
- Click at the point in the proof where the comment should be inserted.
- Type the comment into the box that appears.

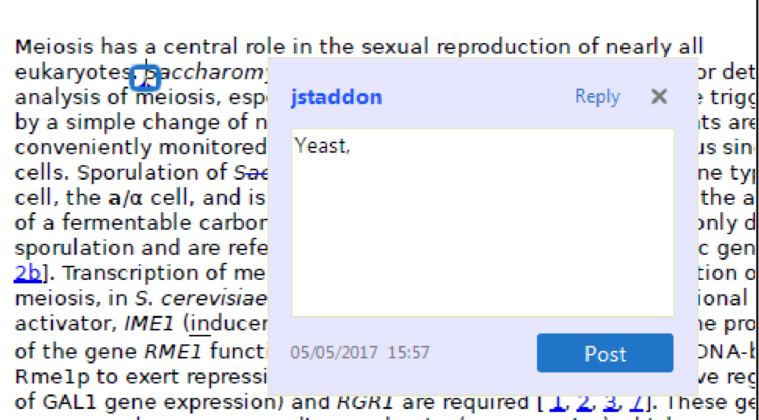

5. Attach File Tool – for inserting large amounts of text or replacement figures.

Inserts an icon linking to the attached file in the appropriate place in the text.

How to use it:

- Click on .
- Click on the proof to where you'd like the attached file to be linked.
- Select the file to be attached from your computer or network.
- Select the colour and type of icon that will appear in the proof. Click OK.

The attachment appears in the right-hand panel.

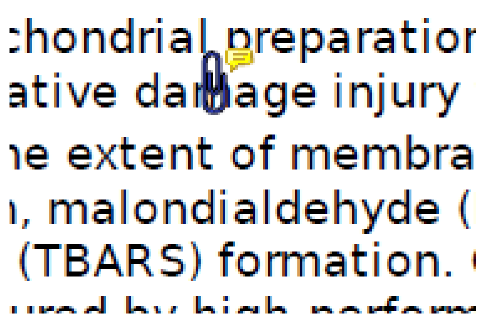

6. Add stamp Tool – for approving a proof if no corrections are required.

Inserts a selected stamp onto an appropriate place in the proof.

How to use it:

- Click on .
- Select the stamp you want to use. (The Approved stamp is usually available directly in the menu that appears. Others are shown under *Dynamic*, *Sign Here*, *Standard Business*).
- Fill in any details and then click on the proof where you'd like the stamp to appear. (Where a proof is to be approved as it is, this would normally be on the first page).

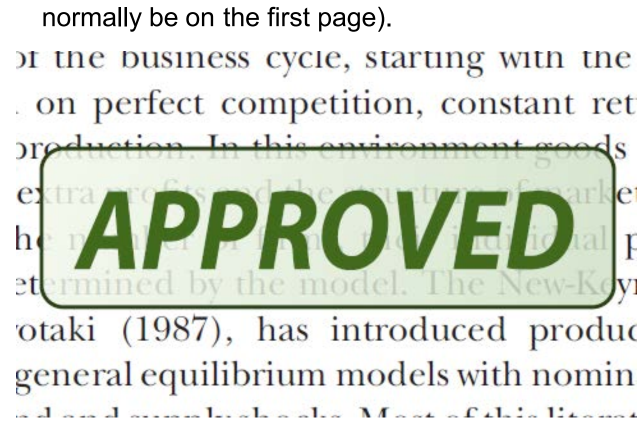

Drawing tools available on comment ribbon

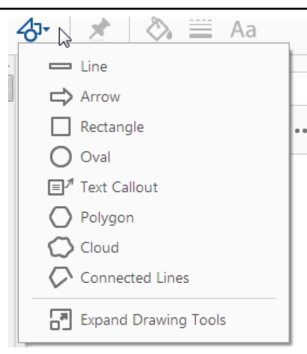

7. Drawing Markups Tools – for drawing shapes, lines, and freeform annotations on proofs and commenting on these marks.

Allows shapes, lines, and freeform annotations to be drawn on proofs and for comments to be made on these marks.

How to use it:

- Click on one of the shapes in the Drawing Markups section.
- Click on the proof at the relevant point and draw the selected shape with the cursor.
- To add a comment to the drawn shape, right-click on shape and select *Open Pop-up Note*.
- Type any text in the red box that appears.

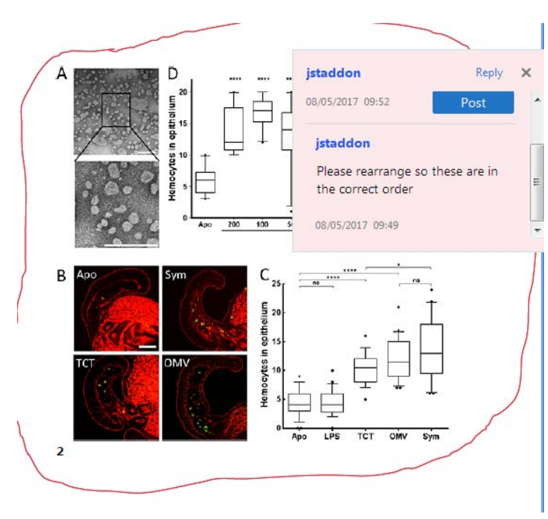

For further information on how to annotate proofs, click on the Help menu to reveal a list of further options:

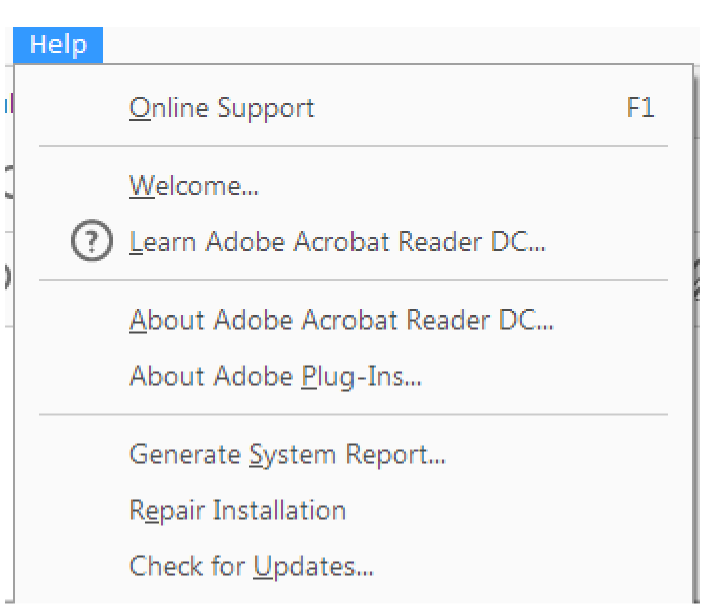

WILEY

Author Query Form

Journal: MRM

Article: 27143

Dear Author,

During the copyediting of your manuscript the following queries arose.

Please refer to the query reference callout numbers in the page proofs and respond to each by marking the necessary comments using the PDF annotation tools.

Please remember illegible or unclear comments and corrections may delay publication.

Many thanks for your assistance.

Query References	Query	Remarks
AQ1	AUTHOR: AUTHOR: Please confirm that given names (red) and surnames/family names (green) have been identified correctly.	
AQ2	AUTHOR: AUTHOR: Please review all affiliations and confirm or amend. Note that journal style asks that you provide site/location name, city, state/province, and country where needed for each affiliation per journal style.	
AQ3	AUTHOR: AUTHOR: Please confirm that (1) the "Funding information" footnote is correct as set; (2) that the correspondence footnote is correct as set; and (3) if desired, please provide the corresponding author's Twitter handle (@handle).	
AQ4	AUTHOR: AUTHOR: Would you please rework "…as by contrast to the latter it benefits from the SNR advantages arising from Fourier integration." for clarity	
AQ5	AUTHOR: AUTHOR: Please clarify if you are referring to Figure 2 or Figure 3.	
AQ6	AUTHOR: AUTHOR: Please rework the sentence, "While in their original single-shot implementation, both SPEN and xSPEN were affected by a progressive T_2 spatial weighting, phase-encoded xSPEN is devoid from such spatially-dependent contrast effects by virtue of its FT-based nature." for clarity.	
AQ7	AUTHOR: AUTHOR: Please provide manufacturer's location (i.e., city and state/country) at first mention for all manufacturer's per journal style.	
AQ8	AUTHOR: AUTHOR: Please confirm that (1) this article contains Supporting Information and (2) the item(s) is/are cited in the correct locations.	
AQ9	AUTHOR: AUTHOR: Please rework the sentence, "Note that because of the full sampling, the multi-scan sequence performs of the k-domain, these data corresponds to a lower resolution image, rotated in space" for clarity.	
AQ10	AUTHOR: AUTHOR: Please define "FTd" at first mention.	
AQ11	AUTHOR: AUTHOR: Would you please rework "…so would cropping a small length of the y′ data allows one to reinstate the original one-to-one y/y′ correspondence, and hence the correctness of the procedure introduced in Figures 2B and 3." for clarity	
AQ12	AUTHOR: Author: If desired, please provide the corresponding author's Twitter handle (@handle).	
AQ13	AUTHOR: Please confirm that given names (red) and surnames/family names (green) have been identified correctly.	

Funding Info Query Form

Please confirm that the funding sponsor list below was correctly extracted from your article: that it includes all funders and that the text has been matched to the correct FundRef Registry organization names. If a name was not found in the FundRef registry, it may be not the canonical name form or it may be a program name rather than an organization name or it may be an organization not yet included in FundRef Registry. If you know of another name form or a parent organization name for a not found item on this list below, please share that information.

FundRef name	**FundRef Organization Name**
Israel Science Foundation	Israel Science Foundation
EU through ERC-2016-PoC	[NOT FOUND IN FUNDREF REGISTRY]
Federal German Ministry for Education and Research	[NOT FOUND IN FUNDREF REGISTRY]
Kimmel Institute for Magnetic Resonance; Perlman Family Foundation	[NOT FOUND IN FUNDREF REGISTRY]
Minerva Foundation	Minerva Foundation
Weizmann Institute of Science	Weizmann Institute of Science
European Commission	European Commission

Received: 11 September 2017 | Revised: 28 January 2018 | Accepted: 29 January 2018

DOI: 10.1002/mrm.27143

FULL PAPER

Magnetic Resonance in Medicine

Phase-encoded xSPEN: A novel high-resolution volumetric alternative to RARE MRI

AQ1AQ13 **Zhiyong Zhang**[1] | **Michael Lustig**[2] | **Lucio Frydman**[1]

AQ2 [1] Department of Chemical and Biological Physics, Weizmann Institute of Science, Rehovot, Israel

[2] Department of Electrical Engineering and Computer Sciences, University of California, Berkeley, California

Correspondence

AQ3 Lucio Frydman, Department of Electrical Engineering and Computer Sciences, University of California, Berkeley, CA 94720.

AQ12 Email: lucio.frydman@weizmann.ac.il.

Funding information

Israel Science Foundation, Grant/Award Number: 795/13; EU through ERC-2016-PoC, Grant/Award Number: 751106; Federal German Ministry for Education and Research, Grant/Award Number: 712277; Kimmel Institute for Magnetic Resonance; Perlman Family Foundation

Purpose: To develop a rapid, non-CPMG high-resolution volumetric imaging approach, exhibiting a speed and in-plane resilience to field inhomogeneities comparable to RARE/turbo-spin-echo (TSE) while endowed with unique downsampling characteristics.

Methods: A multi-scan extension of cross-term spatiotemporal encoding (xSPEN) is introduced and analyzed. The method simultaneously yields k_y/k_z data containing low and high frequency components, as well as transposed, low-resolution *z*/*y* images. This dual *k*-/spatial-domain information is captured by a multi-scan procedure that phase-encodes k_y while simultaneously slice-selecting *z*. A reconstruction scheme converting this information into high resolution 3D images with fully multiplexed volumetric coverage is introduced and exemplified.

Results: Phase-encoded xSPEN was tested by human brain imaging at sub-mm resolutions. The method exceeded 2D TSE's sensitivity by factors of ≈3–4, while providing similar resolution and SNR as 3D TSE in ≈50% acquisition times. The method's contrast is dominated by T_2 and is free from "bright-fat" effects associated to spin-echo trains. Further acceleration is enabled by the method's downsampling abilities. Tradeoffs between encoding time, number of measurements, spatial resolution, SNR, and artifact levels are also laid out.

Conclusion: A new MRI strategy is introduced delivering high in- and through-plane resolutions while enjoying full Fourier multiplexing, leading to fast acquisitions with high SNR.

KEYWORDS

cross-term spatiotemporal encoding, downsampling, high definition resolution enhancement, 3D MRI, turbo spin-echo

1 | INTRODUCTION

Numerous MRI approaches aim at achieving the highest possible anatomical resolution in minimal scanning times, including fast spin- and gradient-echo techniques, steady-state low flip angle acquisitions, and multi-echo/multi-gradient approaches.[1] The latter in particular form the basis of multi-slice 2D turbo spin-echo (TSE), routinely used in MRI exams of animals and humans as optimal compromise between image quality and scanning time. These methods usually afford higher in- than through-plane resolutions because of their reliance on slice-selective pulses. Extensions to 3D TSE and fast spin-echo experiments can make up for this deficiency,[2–4] yet they are less widespread than their slice-selective counterparts because of their demand for long-echo-trains, associated with image blurring or mixed contrast. 3D TSE's high SAR also results in lengthier acquisition times. Imaging methods can be further accelerated by echo planar strategies,[5,6] yet the relatively low bandwidth(s) of the phase-encoded dimension(s) that these experiments involve makes them susceptible to field distortions. Recent years have seen the introduction of methods that, based on a spatiotemporal encoding (SPEN), can deliver single-scan single-slice images with higher robustness to field inhomogeneities than their EPI counterparts.[7–12] Unlike what happens in conventional *k*-based scans, SPEN experiments read out their images in direct, physical space. To do so, swept pulses and gradients are used to imprint a non-linear phase during an initial encoding process, which then provides a focal point for a subsequent, gradient-driven image probing. In their original SPEN implementation this phase involved a quadratic, $\phi = Cy^2$ modulation,[10,13] for which the signal from anywhere, but the center of the parabola is dephased; more recently, an alternative cross-term (xSPEN) procedure was introduced whereby the phase modulation takes a hyperbolic, $\phi = Cy \times z$ profile.[12,14] As a result of such pre-acquisition phase the signal received will be dominated by the saddle point at the center of an hyperbola. An unusual situation then arises whereby applying either G_a^y or G_a^z acquisition gradients will spatially translate this saddle point and unravel, respectively, the $\rho(z)$ or the $\rho(y)$ spatial profiles through the excited slab/slice. The xSPEN sequence on which we hereby focus relates to the second of these options; i.e., on the application of a *z*-axis gradient to unravel a $\rho(y)$ profile. The fact that the exact geometry of the *z*-gradient plays a secondary role in unraveling $\rho(y)$ serves as basis of xSPEN as a single-shot 2D imaging approach that avoids noticeable in-plane chemical shift or other field inhomogeneity distortions. This capability is valuable when considering single-shot 2D acquisitions in the presence of B_0 heterogeneities,[15] known to severely distort basic functional and diffusivity studies.[16,17]

The physical basis of how the application of an acquisition gradient allows one to read, in direct space and without the need for a Fourier transform (FT), the spins' profile along an orthogonal axis, was introduced in Zhang et al.[12] The image domain sensitive-point analysis in that study is intuitive, but does not portray the whole story. For example, in the case of the original SPEN quadratic encoding, the resulting spatially encoded image was blurred by a quadratic phase kernel that extended beyond the usual *sinc*-kernel of *k*-based encoding, requiring super-resolution/deconvolution procedures to achieve an optimal image resolution.[11,18–23] Similarly, xSPEN will have an associated point-spread function mixing *y* and *z* features around its hyperbolic saddle point, leading to the fact that data in the k_y/k_z plane will appear as a transposed, low-resolution *z*/*y* image. This dual spatial-/*k*-domain information content of xSPEN is important because it highlights certain "complementarity" in the method, whereby the application of a gradient will probe the spin density ρ along its own direction (*k*-domain sampling) but also reveal a profile along an orthogonal direction (spatial-domain representation). As a result of this complementarity, it follows that (1) to capture image information in *y* or *z* it is necessary to sample a suitably dense and wide grid in k_z and k_y, as these variables will also act as spatially-sensitive 3D imaging points, (2) *k*-space sampling requirements can still be used to derive the final resolution and image sensitivity based on traditional Nyquist criteria, and (3) unusual relations will emerge in terms of scanning time, resolution, FOV, and SNR among the *y*- and *z*-domains, particularly on downsampling the *k*-values. In this work, we further develop these topics. The following section introduces a multi-scan, phase-encoded 3D version of xSPEN and a novel reconstruction scheme that exploits this experiment's hyperbolic phase encoding. We then discuss the sensitivity, FOV, resolution, contrast, and downsampling characteristics of the new method. The Results section provides a series of high-resolution multi-scan xSPEN imaging examples and analyzes their sensitivity vis-à-vis commonly used multi-slice 2D fast spin-echo (FSE/TSE/RARE) and multi-slab 3D fast spin-echo MRI techniques. We conclude with a discussion of the limitations and further potential of this new imaging technique.

2 | METHODS

2.1 | Principles of phase-encoded multi-scan xSPEN MRI.

Figure 1A illustrates the xSPEN strategy that we introduced for single-shot 2D acquisitions free from noticeable in-plane offset distortions, over *x* and *y* fields-of-view FOV_x, FOV_y. This sequence applies a G_z gradient for the initial excitation of a slab-width L_z. Two linearly-swept adiabatic inversion pulses[13,24] of bandwidth BW and duration $T_p = T_a/2$—with $BW = |\gamma G_z L_z| + |\gamma G_y FOV_y|$ and T_a denoting the eventual acquisition time—are then applied in conjunction with a bipolar $\pm G_y$ gradient. This leads to the $\Phi_e = -Cy \times z$ hyperbolic phase modulation characterizing xSPEN, with $C = \frac{T_a \times \gamma G_y \times \gamma G_z}{\pi \times BW}$ a spatiotemporal encoding constant under the experimentalist's control. The saddle-shaped phase profile associated to this encoding leaves solely a sensitive region fulfilling $\frac{\partial \varphi}{\partial y} = \frac{\partial \varphi}{\partial z} = 0$ where substantial cancelation among neighboring spins does not occur; over the course of the signal acquisition the continued action of G_z displaces this saddle-shaped profile, progressively probing $\rho(y)$. The mechanism by which the constant application of a G_z gradient delivers, in direct physical space, an image free from inhomogeneities along an orthogonal axis, has been discussed in detail elsewhere.[12] In brief, this behavior follows from calculating the time-domain signal that will be originated in such experiment, which for a thin enough slice can be written as

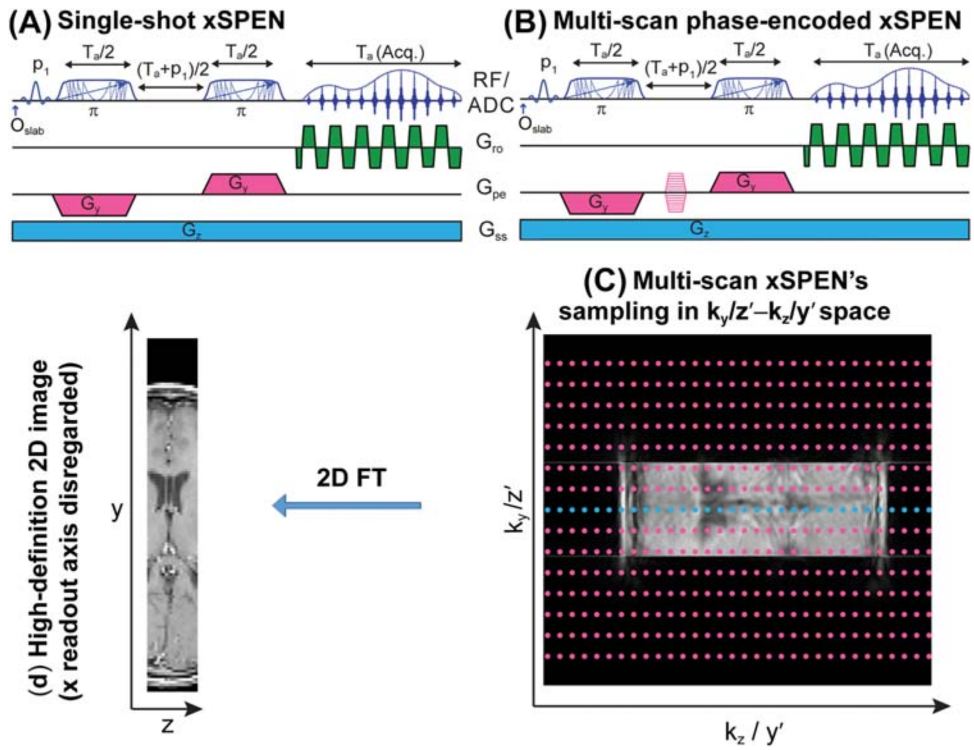

FIGURE 1 (A) Original single-shot xSPEN sequence mapping $\rho(x,y')$ for a single z-slab. (B) Phase-encoded multi-scan xSPEN sequence introduced in this work. (C) Simulated *k*-domain data arising from the sequence in (B) along the (k_y,k_z)-domain; notice the low-resolution rendition of the brain being imaged. Blue dots indicate what would be collected in a single-shot xSPEN acquisition, corresponding to the y′ profile for a particular z slice position; magenta dots indicate the fully phase-encoded xSPEN space sampled by the multi-scan sequence (B). (D) Image arising on applying a 2D FT to the signal $S(k_y,k_z)$, followed by a magnitude calculation. Note that because of the full sampling, the multi-scan sequence performs of the *k*-domain, these data corresponds to a lower resolution image, rotated in space

AQ9

$$S(k_z) \propto L_z \int_r \rho(x,y) \cdot \text{sinc}\left[(-Cy+k_z)\frac{L_z}{2}\right] dxdy. \quad (1)$$

The *sinc* modulation in Eq. (1) means that the *S*-signal will probe, linearly in the wavenumber $k_z = \gamma G_z t$, the spin density along *y*. In the full single-shot 2D experiment in Figure 1A, this 1D probing is executed in conjunction with an oscillating $\pm G_x$ gradient applied along an orthogonal readout dimension, that samples the k_x-axis in an echo planar manner. Given the conventional way in which this *x*-axis is involved, all normal manipulations (partial sampling, weighting, etc.) can be applied. Because of its standard nature we ignore this dimension for most of the remaining treatment.

When considering the extension of these principles to multi-scan volumetric scanning, a number of options arise. One is multi-slicing the original single-shot, slice-selective 2D technique. A problem associated with doing so relates to the limited resolution that one would obtain: along the *z* axis this would equal the pulse-selected slice width L_z, whereas along the *y* direction resolution would be given by the width of the *sinc* in Eq. (1). This *sinc* essentially acts as the point-spread-function of the *y*-axis sampling, for which it can be shown that resolution will be given by FOV_y divided by the time-bandwidth product $Q = T_p.BW$ of the frequency-swept encoding pulses.[12] Therefore, unless ready to afford long acquisition times (with concomitant diffusion- and relaxation-driven sensitivity losses) or large excitation bandwidths (with concurrent SAR penalties) there is a limit to how large Q can be made. One can thereby visualize k_z as sampling a "low-resolution" rendering of $\rho(y)$, a $\rho(y' = k_z/C)$ profile whose definition we would like to increase. One possibility to do so could arise from the addition of a conventionally looped, phase-encoding G_y gradient, into the sequence (Figure 1B), a multi-scan phase-encoded (PE) xSPEN variant that will be the focus of this study. FT along the k_y dimension resulting from incrementing this phase-encoding then provides FOV_ys and resolutions Δy along the usual guidelines of Nyquist criteria. However, the bilinear kernel e^{iCyz} that is also encoding all spins in this variant, leads to another peculiar situation. In the same manner as it was shown that a k_z wavenumber could read out the y' profile, this 2D xSPEN scanning of a k_y axis leads to an analog of Eq. (1)

$$S(k_z) \propto FOV_y \int_r \rho(x,y) \cdot \text{sinc}\left[(-Cz+k_y)\frac{FOV_y}{2}\right] dxdz, \quad (2)$$

and thereby to the sampling, in direct physical space, of a low resolution $\rho(z' = k_y/C)$ profile. In fact the resolution of this indirectly-sampled z' image will be given, like its direct-domain sampling y' analog, by the time-bandwidth characteristics of the same encoding pulses. This ability to sample low-resolution y'/z' spatial dimensions using G_z/G_y gradients is a consequence of the acquisition kernel imposed by the e^{iCyz} hyperbolic phase modulation: unlike what happens in conventional MRI, where such kernel is given by a well-localized 2D *sinc* k-domain function where orthogonal spatial dimensions are decoupled, xSPEN entangles the y- and z-domain information and spreads the k-space sampling from traditional MRI's well-localized situation, into a 2D box-like shape. Figure 1C illustrates an unusual consequence of this feature on a 2D human brain scan: note the "swapping" of the sampling k-axes and of the post-Fourier spatial data, with the former strongly resembling a rotated version of the latter.

2.2 | Processing the phase-encoded xSPEN data

The fact that in this experiment the k-domain data is similar to the spatial 2D image is reminiscent to what happened with the original SPEN quadratic kernel.[13] This notwithstanding, the fact remains that the encoding carried out by G_y and G_z in the sequence shown in Figure 1B, will also actively sample the 2D k_y/k_z-space. Hence, aside from an overall e^{iCyz} phase factor deriving from xSPEN's hyperbolic phase modulation, 2D FT of data that have been suitably sampled in the k_y/k_z-plane, will provide a conventional 2D $\rho(y,z)$ MR image. Figure 1D evidences this with the data arising by 2D FT (+magnitude calculation to remove the residual hyperbolic phase) of the low-resolution $\rho(y' = k_z/C,\ z' = k_y/C)$ "image" introduced in Figure 1C. Notice the higher resolution of the FT-derived image both along the PE as well as along the slice/slab-selective (SS) dimension, which is dissected into Q points by the G_z gradient. Besides a higher resolution, this FT-originated image is also characterized by a better sensitivity than the xSPEN-rasterized image, as by contrast to the latter it benefits from the SNR advantages arising from Fourier integration.

The redundancy that in terms of information, content arises between the phase-encoded signal $S(k_y)$ and the k_z-based decoding of the $\rho(y')$ image, opens an option to speed up these multi-scan acquisitions. To appreciate this, consider the lengthier sampling occurring along the PE k_y axis, whose resolution will be given by the largest k_y^{max} value sampled, and whose span is given by $\Delta k_y = 1/FOV_y$. Even disregarding the possibility of accelerating experiments by parallel MRI,[25–28] the fact that the full FOV_y is evaluated in a folding-free, lower resolution fashion throughout the direct-domain $k_z/C = y'$ acquisition opens unusual downsampling possibilities. Indeed, skipping k_y points will lead to folding over among different regions throughout the FOV_y range. The fact that this information is available along the orthogonal $k_z/C = y'$ axis makes it possible to unfold these artifacts and recover the full y range—while still enjoying the full resolution arising along this axis from the k_y^{max} sampling. Although there is more than 1 avenue to perform this kind of unfolding, Figure 2 shows an alternative that we chose for highlighting the potential as well as the compromises of this approach. Consider first a scenario involving a full dense sampling of the relevant 2D k-space. As discussed in Figure 1, the simplest avenue to obtain from these data a high definition image is by performing a 2D FT. Figure 2A shows an alternative way of arriving at the same image in a series of steps that explicitly remove the hyperbolic phase by a number of shearing transformations. Involved in the first step, is a 1D FT along k_y, leading to a correlation between a high-definition y-axis and a low-resolution image sampled by the $k_z/C = y'$ variable. This is represented in the second left-most image of Figure 2A, possessing a clear diagonal arising from the ensuing y/y' image correlation (for ease of representation, we assume a zero-padding of the k_z axis that places this diagonal along a unity-value slope). Colored traces showing different k_z-domain echoes, which in this mixed-phase interferogram will encode the spatial information along the slice-selected domain, are also illustrated in this experimental panel. The high-resolution y-image arising along the y/y' diagonal can be placed along a horizontal dimension via a shearing transformation of the 2D data set (Figure 2A, center). Although this will result in losing the "pure" k_z-encoding along the orthogonal axis, this can be remedied by a second, orthogonal shearing transformation leading to the echo disposition illustrated in the second right-most interferogram of Figure 2A. From this data set, an additional 1D FT along k_z (now placed along the vertical axis because of the shearing processes) will afford the high-definition 2D image being sought.

Consider now the extension of the same procedure to a downsampled case, where phase-encoded lines were periodically skipped for the sake of speeding up the multi-scan acquisition (Figure 2B). Following the first FT versus k_y, a PE that has been downsampled by a factor R_y will lead to foldovers along the resulting y axis (Figure 2B, left, red and yellow echoes). Notice, however, that it will incur in no resolution sacrifices along this axis because k_y^{max} has not changed. Normally such R_y-folded images cannot be disentangled without additional help (i.e., from multiple receiving coils). Additional information, however, is present in the xSPEN acquisition, because when correlated against the $k_z/C = y'$ information only the folding-free data will lie along a unity diagonal. The first of the shearing transformations introduced in Figure 2A can clearly disentangle this information, providing the folding-free profile in the middle horizontal line in the center panel of Figure 2B. A second shearing transformation followed by a cropping out of the spurious

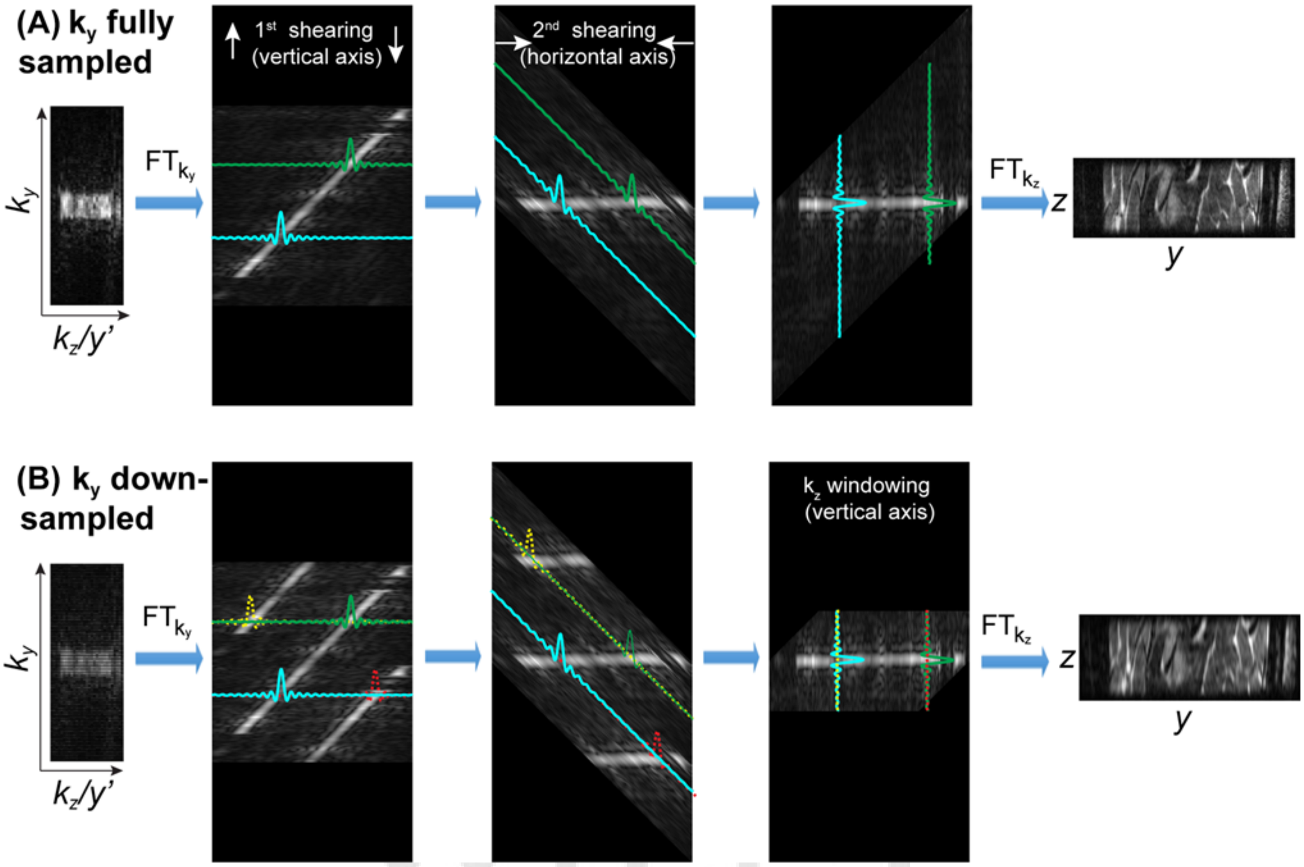

FIGURE 2 Reconstruction diagram proposed for processing phase-encoded xSPEN with or without downsampling, leading to the same kind of Fourier magnitude image. (A) Reconstruction for a fully sampled data set. (B) Reconstruction of a data set that has been downsampled in k_y (notice that every other k_y line is missing in the left-most starting set). The foldovers that this originates are represented by dashed yellow and red echoes, which are removed by the indicated procedures. See the main text for further details

folded information and by a second FT therefore leads to a full-definition y-axis information.

While exploiting its additional k_z/y' information for obtaining a folding-free image despite the downsampling, Figure 2 shows that skipping PE lines will bring a penalty—not along the y but along the SS axis. At first sight, this may seem counterintuitive because this was not the downsampled axis. Notice, however, that as a result of the k_y downsampling, echoes that were overlapping along their k_z-domain will be cropped out by the processing in Figure 2B; this will reduce their support by a factor R_y, and hence lower their z-axis resolution by this same factor. The "xSPEN picture" that assigns the sampling of the k_y/k_z axes to a rasterization of the z/y domains makes this prediction, as missing elements in the former equates to skipping positions in the latter. An experimental verification of this can be appreciated by comparing the leftmost panels in Figure 2, where the loss in z resolution on downsampling k_y is evident. In fact, there is another z-imaging penalty associated to the downsampling that may also lead to a special kind of k_z-domain foldover involving high frequency components aliased from non-diagonal y positions that are not eliminated by the data cropping (see color-coding of the k_z echoes in Figure 2B for a graphic explanation). The precise artifacts arising from this k_z overlap will depend on the features within the z-domain slab and on the "tightness" of the hyperbolic encoding kernel. Specifically, if a targeted z slab is to be defined by a limited number of Fourier coefficients N_{slab}, then it can be proven that no compromises will be made as long as $N_{slab} \leq Q/R_y$, where Q is both the aforementioned time-bandwidth product defining the hyperbolic encoding as well as the number of $\pm$readout echoes collected (i.e., the number of points ideally sampled along k_z). As further illustrated below, this will be the lower limit over which downsampling can be executed while leaving a nearly lossless reconstruction.

Figure 3 presents additional details regarding the procedure introduced in Figure 2, this time taking into consideration the presence of the third, readout domain. As mentioned, this involves an EPI-like $\pm k_x$ train of gradient oscillations on which a regular FT is applied to map the x profile information. The y' and z' axes associated to the k_z and k_y domains are also indicated in the figure. Notice that the 2 shearing transformations introduced in Figure 2 are carried out by 2 separate phase corrections imparted in their conjugate Fourier domains—hence the mentioning of 2 2D

F3 AQ5

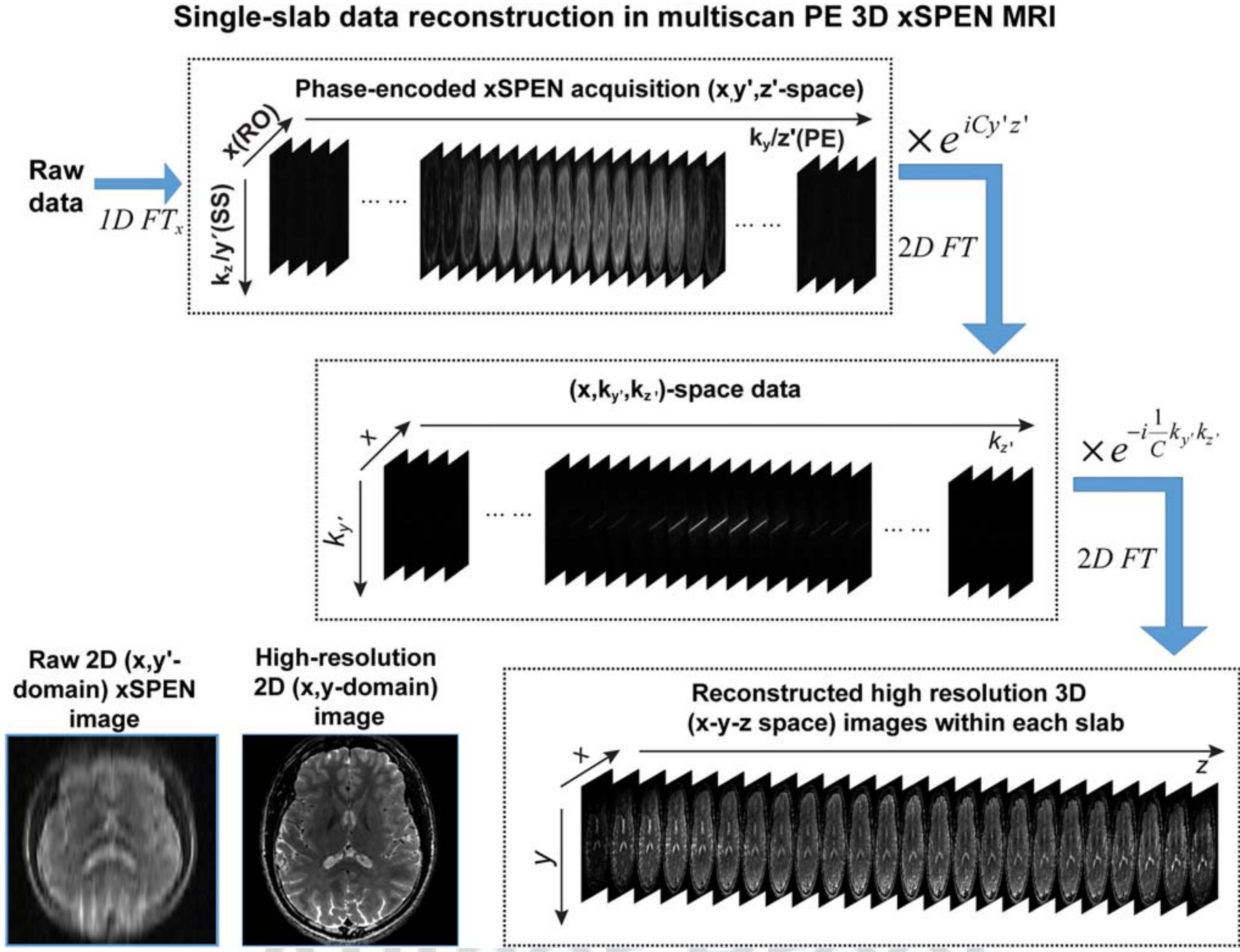

FIGURE 3 Details of the reconstruction procedure introduced in Figure 2, illustrated for a given xSPEN phase-encoded slab acquired with a spatiotemporal encoding factor C. To obtain the ensuing high resolution images, the readout dimension (encoded by G_x) is first FTd, and the illustrated steps are used to arrive to the final high resolution 3D image within each slab. These steps reflect the shearing procedures illustrated in Figure 2, realized here via C-dependent phase multiplications in the relevant mixed k/r-spaces. The bottom left images compare the resulting high resolution images with the low resolution counterpart arising in the ($y' = k_z/C, x$)-domain

AQ10

FT steps, instead of the 1D FTs as in Figure 2. The zero padding mentioned as the initial step in Figure 2 and the windowing/cropping mentioned in the last step of that figure are omitted in Figure 3 for simplification, but they are actually required as part of the processing.

2.3 | FOV and resolution in multi-scan xSPEN MRI.

As was the case with its single-shot counterpart,[12] the FOVs that will be observed in multi-scan PE xSPEN will be defined by the characteristics of the encoding swept pulses. At the same time, additional FOV and resolution considerations will be dictated by the sampling and the FTs implemented on the various k-variables. Further effects will arise from potential k_y downsampling procedures. To consider all this, we neglect, as before, the conventional RO domain and focus on events defining images in the y/z plane. As discussed in Figure 4 of Zhang et al.,[12] the initial SS plus the 2 ensuing swept pulses will define, in unison with the various G_y/G_z gradients, a diamond-like targeted shape in this plane. Red polygons are shown in Figure 4 under idealized conditions that disregard field inhomogeneity or chemical/susceptibility shifts, as well as non-idealities of the adiabatic sweeps that are considered in more detail in the Supporting Information S4. In the original single-shot implementation, the y-axis information emerged on sampling k_z, and therefore "zooming in" could be carried out trivially. In the present case, however, different scenarios emerge depending on whether the object to be imaged is targeted by the FOV_y arising from the k_y encoding, or it is not (Figure 4). If the imaged object is entirely located within the predefined $FOV_y \times L_z$ region (Figure 4A), all the previously derived multi-scan xSPEN arguments will hold. By contrast, if zooming on an object that extends beyond the predefined FOV_y (Figure 4B), foldover artifacts may arise along the y-axis. This reflects the

F4

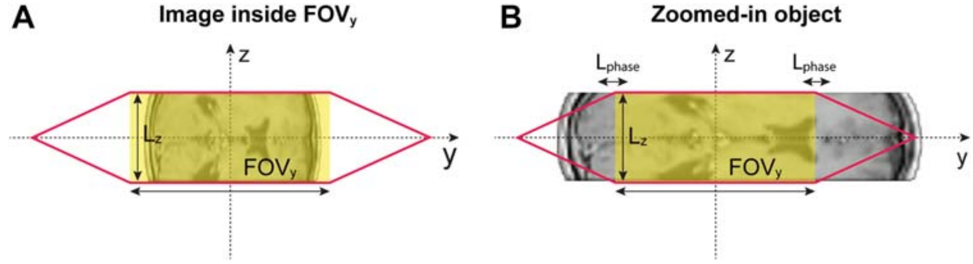

FIGURE 4 Two scenarios arising in a multi-scan xSPEN MRI experiment targeting a $FOV_y \times L_z$ region (yellow box). The red polygon shows the slab defined by the RF pulses themselves,[12] whereas the grey images illustrate a putative object. Notice that in common imaging cases, $FOV_y \geq 10xL_z$. (A) The whole object is located within the $FOV_y \times L_z$ region defined by the k_y/k_z sampling parameters. (B) "Zoomed-in" scan where the imaged object extends beyond the predefined $FOV_y \times L_z$ region. In this case, a slightly larger $FOV = L_{phase} + FOV_y$ is required for imaging the desired FOV_y without folding artifacts, where $L_{phase} = FOV_y/Q$ is generally much smaller than FOV_y for common (Q ≈ 20–40) settings

fact that the xSPEN k_z/y' dimension will sample y information arising from object components outside the FOV_y without folding; hence the occurrence of a k_y-driven folding would make the procedure introduced in Figure 2 inconsistent.

The y-axis folding effect will be limited by the selectivity of the spatiotemporal encoding to a spatial extent $L_{phase} = FOV_y/Q$, which is generally much smaller than FOV_y for commonly used (Q ≈ 20–40) settings. Expanding by an additional factor 1/Q, the FOV_y extent targeted by the k_y phase encoding will solve this folding problem, alternatively, so would cropping a small length of the y' data allows one to reinstate the original one-to-one y/y' correspondence, and hence the correctness of the procedure introduced in Figures 2B and 3. Figure 4B shows that even with k_y oversampling, the profile along the y axis may be slightly affected by the non-uniform thickness of the z profile; this, however, is a negligible effect for the relatively thin slabs targeted in most imaging experiments. It is worth noting that from a practical perspective, a small oversampling along the k_z acquisition is also usually useful in dealing with non-idealities in the slab selection process.

The resolution and line shape characteristics of multi-scan xSPEN for a fully-sampled k_y acquisition can be appreciated from Figure 2A. This shows that the k_z echoes will appear shifted for different y positions, with a minimal extent of $|k_z|$ sampling occurring for $y = 0$ and a prediction of dispersive-free line shapes and a $\Delta z = L_z/Q$ resolution for this symmetric-echo case. For other y-values, the echoes will be asymmetrically placed thereby leading to potential dispersive components; however, given that an object's image should be real, these components can be eliminated by a complex conjugation that restores the full symmetry to the k_z echoes.[29,30] Further, by doing this asymmetric-to-symmetric echo conversion, the z resolution will be improved in a y-dependent fashion, ranging from the aforementioned Δz at the center of FOV_y, to $\Delta z = L_z/2Q$ at the edges. Conversely, should the data be processed so that the k_y echoes appear shifted for different z positions, the y resolution would span from a minimum $\Delta y = 1/k_y^{max}$ value at the center of the z-slab, to an improved $\Delta y = 1/(k_y^{max} + Q/FOV_y)$ value (after a complex-conjugate constrained reconstruction) at the edges of the z axis. In the case of a downsampled k_y acquisition, the unfolded y information will still be accessible from the reconstruction shown in Figure 2B. The y-axis resolution will then stay identical as with the full k_y sampling counterpart, whereas the z resolution will be decreased and potential artifacts may arise because of the aforementioned k_z-folding effects. This worsening in the z resolution will be y-independent, and artifacts will depend on the object's characteristics at other y position(s). In general, resolution losses and z-axis artifacts will be negligible if the z features change smoothly, as will usually be the case when dealing with natural objects; alternatively, spurious artifacts will arise if dealing with strong, sharp features. In most objects that we have scanned, the k_z-folding effects brought about by k_y downsampling yields images whose appearance are akin to their fully k_y-sampled counterpart, apart from a "skipping" of intra-slab z-slices. This is again in accordance with the picture of the k_y variable as sampling physical positions along the z direction: downsampling in the former axis will then lead to missing slices in the latter.

2.4 | SNR and contrast considerations

As shown in Figure 1, multi-scan xSPEN can, for a full k_y sampling, reconstruct a conventional y-z image (aside from a phase e^{iCyz}) by 2D FT. This magnitude image will have the same SNR as a fully 3D k-encoded FT-based counterpart (SNR_{FT} in Figure 5), because the FT implemented along xSPEN's k_z axis reinstates a multiplexing advantage that was absent on 2D multi-slice experiments collected under identical resolution and FOV conditions. Increasing the number of scans beyond this value by either repeating scans or by oversampling the phase-encoded axis, will bring about a conventional $\sqrt{N_{scans}}$ (or $\sqrt{N_{oversampling}}$) dependence on the number of averaged scans (or oversampled points). On downsampling the k_y axis, a number of scenarios will arise. As long as artifacts from the aforementioned k_z foldover effects do not

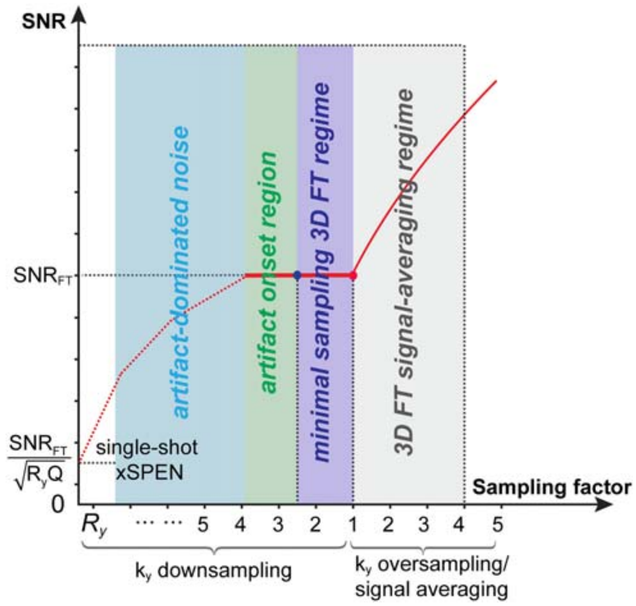

FIGURE 5 Sensitivity (SNR) considerations affecting multi-scan xSPEN MRI as a function of its over/downsampling. SNR_{FT} represents the sensitivity that—if ignoring for simplicity field inhomogeneity, T_2, and diffusion-decay effects—will characterize a fully-sampled 3D FT MRI image under identical resolution and FOV conditions. See text for the meaning of the various colors and regimes

arise, the SNR will remain constant—even if the *z*-axis resolution will start to decrease owing to the *z*-skipping effects mentioned above (purple region in Figure 5). At some point, however, the k_y downsampling will start to cause an overlap between the tails of the various k_z acquisitions, leading to artifacts that may eventually overcome noise as the main factor controlling the image's sensitivity (Figure 5, in green). Eventually, in the $k_y = 0$ limit, the experiment reverts to single-shot xSPEN; this acquisition does not attempt to resolve anymore the intra-slab *z* structure, and because all multiplexing advantages are lost the sensitivity decreases down to a factor $\sqrt{R_y Q}$.

AQ6 While in their original single-shot implementation, both SPEN and xSPEN were affected by a progressive T_2 spatial weighting, phase-encoded xSPEN is devoid from such spatially-dependent contrast effects by virtue of its FT-based nature. There will still be an overall T_2-weighting arising from the pre-acquisition delays—but they will affect the in-plane images uniformly. A diffusion contrast will also affect the images arising from the b ≈ 100 s/mm^2 weighting associated with xSPEN's encoding gradients—yet this will also be a constant. The sole progressive effect will be as a function of the readout echo number (i.e., along k_z). This should result in an intra-slab blurring along *z* although this is relatively minor and was not noticed in the experiments—probably as a result of the relatively short duration and weak G_z gradients associated to the data acquisition process.

2.5 | Experimental

Human volunteers were scanned on Weizmann's 3T Siemens TrioTIM platform using a 32-channel head coil. All experiments were approved by the Internal Review Boards of the Wolfson Medical Center (Holon, Israel) and the Weizmann Institute and were collected after obtaining informed, suitably written consents. The purposes of the experiments were 2-fold: to test the various features derived above for multi-scan 3D xSPEN and to compare the performance of this sequence against alternatives that can provide comparable 3D images in terms of resolution, contrast, and sensitivity. Three sequences were chosen for this comparison, all taken from the scanner's library: 1 based on 2D slab-selective EPI, and the other 2 on turbo spin-echo (TSE) MRI. Given the mm and sub-mm resolutions being sought, the EPI sequence had to be run using multi-scan phase-encoding along the SS axis, as well as multi-shot interleaving along the low-bandwidth (PE) dimension; although these procedures worked on phantoms, they gave consistent artifacts under in vivo conditions (despite the collection and reliance on navigator scans) and hence its resulting images are not presented here. Both multi-slice 2D and phase-encoded 3D versions of TSE were successfully run at the desired resolutions and compared against home-written xSPEN acquisition sequences. In none of the experiments were parallel acquisition, fat suppression, partial FT, or simultaneous multi-slice capabilities implemented: such optimizations have not yet been fully developed for xSPEN, and hence they were left out of the comparisons. Two sets of scan parameters are presented in this study; details on one are shown in Table 1, whereas the multi-scan parameters for the second set included TR = 2s, TE = 81 ms, $FOV_x \times FOV_y =$ 192 × 192 mm^2, in-plane matrix size = 192 × 192, *z*-slab thickness = 12 mm, number of slabs = 16 (i.e., $FOV_z =$ 192 mm), xSPEN time-bandwidth product Q = 24, G_z = 1.57 mT/m, G_y = 0.10 mT/m, echo train length = 29 (≈1.2 × Q; i.e., a 20% oversampling to better resolve the slices within each slab at a 12 mm/24 = 0.5 mm resolution), echo spacing = 1.03 ms, and an initial 15 ms long SLR 90° excitation pulse. The overall scan times of these experiments without downsampling was 6 min 40 s. To explore zooming-in capabilities, small FOV imaging xSPEN experiments were also recorded using the same parameters as above except that G_y = 0.20 mT/m, FOV_y = 96 mm, number of phase encodings = 96, and overall scan time = 3 min 20 s.

3 | RESULTS

Figure 6 illustrates high-resolution features of multi-slab, phase-encoded xSPEN MRI. These images arise from a multi-shot 3D xSPEN acquisition that covered the whole brain using an in-plane resolution of 1 × 1 mm^2 and a

TABLE 1 Sequence parameters for 3D xSPEN, 3D TSE, and 2D TSE experiments

Parameters	PE xSPEN scan 1	PE xSPEN scan 2	3D TSE	2D TSE
Echo spacing (ms)	1.03	1.03	9.88	13.2
Echo train length	29	29	29	29
TR (ms)	2000	4000	4000	8200
TE (ms)	99	99	99	92
Slice/slab thickness (mm)	12	12	12	0.5
Slices/slabs (*N*)	13	13	13	312
Volume (mm^3)	192 × 192 × 156	192 × 192 × 156	192 × 192 × 156	192 × 192 × 156
Resolution (mm^3)	1 × 1 × 0.5	1 × 1 × 0.5	1 × 1 × 0.5	1 × 1 × 0.5
SAR (W/kg)	0.699	0.349	0.719	0.428
Total acquisition time	6 min 24 s	12 min 48 s	16 min 54 s[a]	16 min 30 s[b]

[a]An oversampling factor of 1.5 was applied along the slab dimension of this acquisition to avoid slice folding effects.
[b]Although a single slice image took ≈400 ms to collect, achieving a 156 mm coverage along the SS dimension demanded a large number of slices (312) to be acquired (in 15 concatenations) leading to a minimum TR of 8200 ms.

0.5 mm resolution across the slab dimension. The data were collected without downsampling, using a full $k_x/k_y/k_z$ data set and processed according to the recipe in Figure 3. These images are dominated by a T_2 contrast and lack any noticeable susceptibility or fat–water shift in-plane distortions despite the absence of multiple spin echoes owing to xSPEN's built-in compensation characteristics.[12] Nearly absent as well, are "stitching effects" along the SS axis, owing to the cleanness with which the SLR slab-selective excitation and the subsequent inversion pulses addressed each of the "diamonds" introduced in Figure 4. To ensure this cleanness throughout the full FOV_y, FOV_z extents, the Q-values of the WURST-shaped[24] encoding pulses were increased by ∼35% (see the Supporting Information S4 for further details on the slice selection). An interleaved slab acquisition procedure also ensured long TRs the absence of noticeable T_1-weighting effects (that could be included by shortening the TRs).

Figure 7 and Table 1 compare representative performances of 3D multi-slab PE xSPEN acquisitions against 3D multi-slab PE TSE and 2D multi-slice TSE results collected under as-close-as-possible acquisition conditions. Important criteria maintained throughout these comparisons were equal FOV and resolution along all dimensions; similar T_2-based contrasts among the images were also sought. At first glance, the various whole-brain images shown in Figure 7 look similar, even if slight differences—particularly concerning the fat-derived signals—arise because of the different slab/slice excitation bandwidths of the different experiments. The most noticeable differences among both sets of images arise from "bright fat" artifacts[31] of the kind that usually accompany TSE experiments acquired with long echo trains, effects that

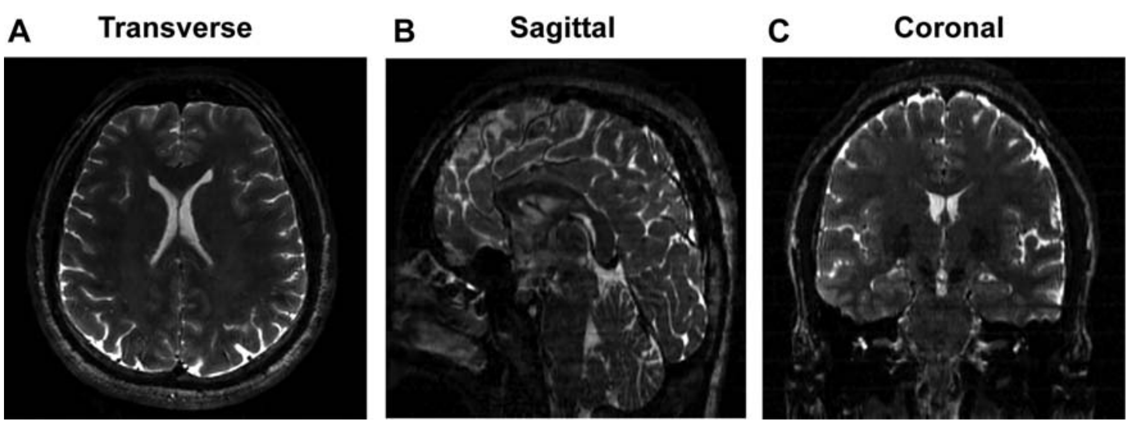

FIGURE 6 Three-plane high-resolution images acquired using multi-slab phase-encoded xSPEN imaging. Multi-slabs were combined based on their weighted slab profiles[35,36] to get sagittal and coronal planes from multiple transverse acquisitions

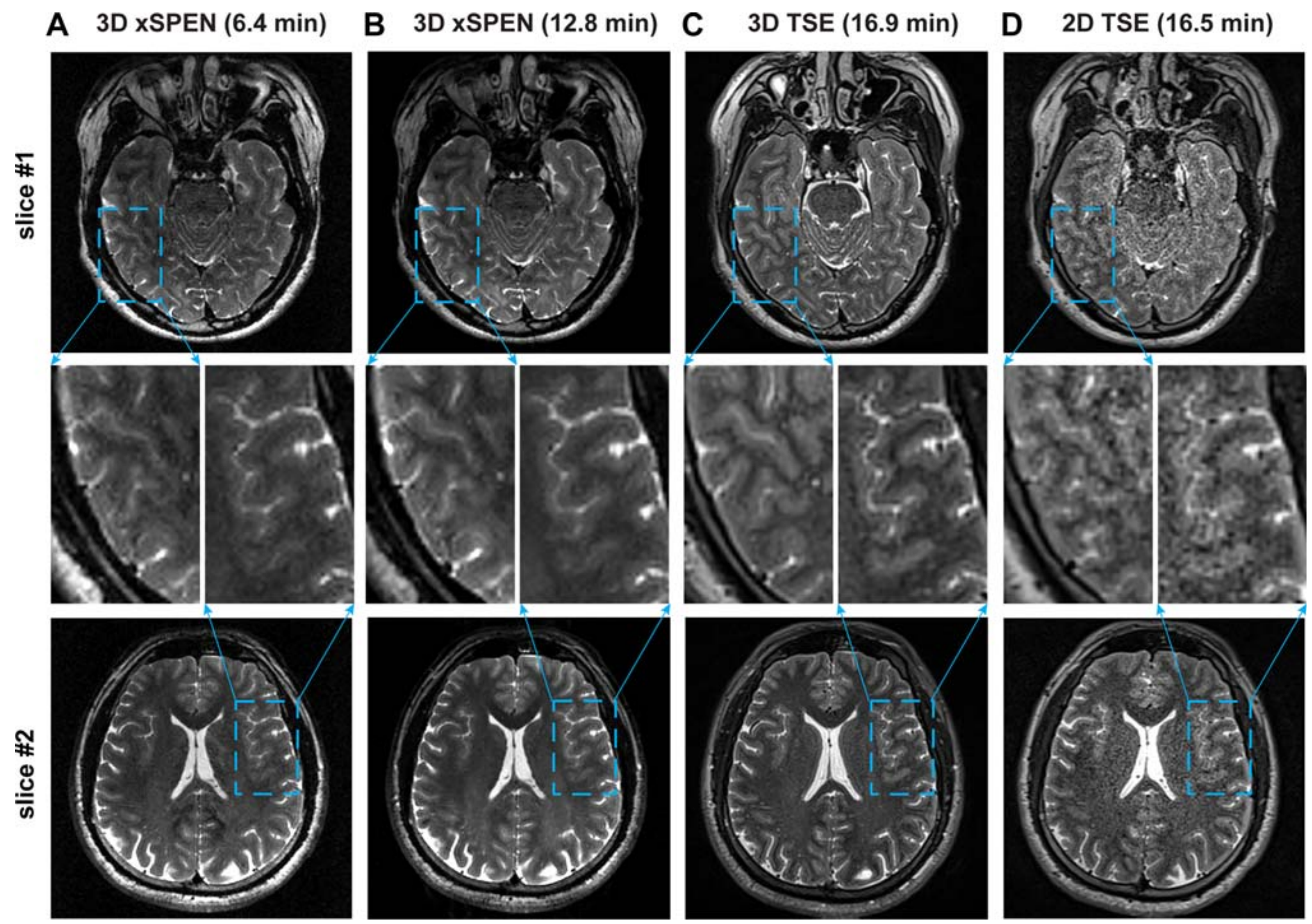

FIGURE 7 Comparison between xSPEN and TSE acquisitions covering a volunteer's whole brain, shown for 2 representative slices and indicating their total scan times. (A and B) Multi-slab 3D PE xSPEN images collected using TRs of 2 and 4 s, respectively. (C) Multi-slab 3D PE TSE images (TR = 4 s). (D) Multi-slice 2D TSE images (TR = 8.2 s). Zoomed images shown in the middle row arise from the light blue marked regions. No downsampling was done in any of the experiments. Further acquisition parameters are detailed in Table 1

are absent in the case of xSPEN. As can be appreciated from the zoomed images in the middle panels of Figure 7, arising from the regions marked by light-blue dashes in the whole-brain slices, a remarkably superior sensitivity characterizes all 3D methods over 2D TSE, thanks to their use of a FT along the SS dimension. The longer acquisition times that 2D TSE needs to achieve the 0.5-mm slice thickness delivered by the 3D methods are also remarkable, reflecting the large number of slices leads needed for covering the whole brain. Moreover, although the sensitivities of 3D TSE and 3D xSPEN are comparable, the minimum TR required by 3D TSE (~3800 ms) is substantially longer than its xSPEN counterpart (~1600 ms) for identical slab settings covering the whole brain. This reflects the longer per-slice acquisition times and the heavier SAR deposition required by 3D TSE per unit time, to cover these large FOVs at these high resolutions (Table 1). By contrast, xSPEN's EPI-based acquisition and its full T_2^*-refocused nature can achieve the same effects, without requiring TSE's trains of rewinding gradients and refocusing pulses.

A quantitative in vivo comparison of SNR among the various PE methods is challenged by the influence of multichannel coil operation,[32,33] as well as because of potentially different motion and diffusion effects. To account for this, the protocol's SNRs were measured on a $NiSO_4$-doped water phantom by repeating them several times identical conditions, without relying on parallel receiving. SNRs were then evaluated as $mean_{r\in ROI}(S(r,\kappa_i)+S(r,\kappa_{i+1}))/stddev_{r\in ROI}\ (S(r,\kappa_i)-S(r,\kappa_{i+1}))$,[32] where the functions *mean*( ) and *stddev*( ) return the mean value and the SD over selected regions of interests, and the κ_i represent repeated measurements. Results of these analyses are presented as Supporting Information S1. These results validate Figure 7 and show that: (1) although an SNR advantage of ≈1.28 × is expected for 3D TSE versus 3D xSPEN because of their different oversampling factors along the slab dimensions (1.5 vs. 1.2) and RO bandwidths (789 vs. 1042 Hz/pixel), a slightly higher gain (1.36×) is experimentally observed, and (2) although an SNR advantage of 4.7 × is expected for multi-scan xSPEN over 2D TSE, reflecting the former's PE steps along slab/slice dimension (29 vs. 1) and different RO bandwidths (1042 vs. 789 Hz/pixel), a slightly lower experimental gain is observed (3.4×). Both of these effects can be traced to xSPEN's exp(−b × D) diffusivity losses, which for

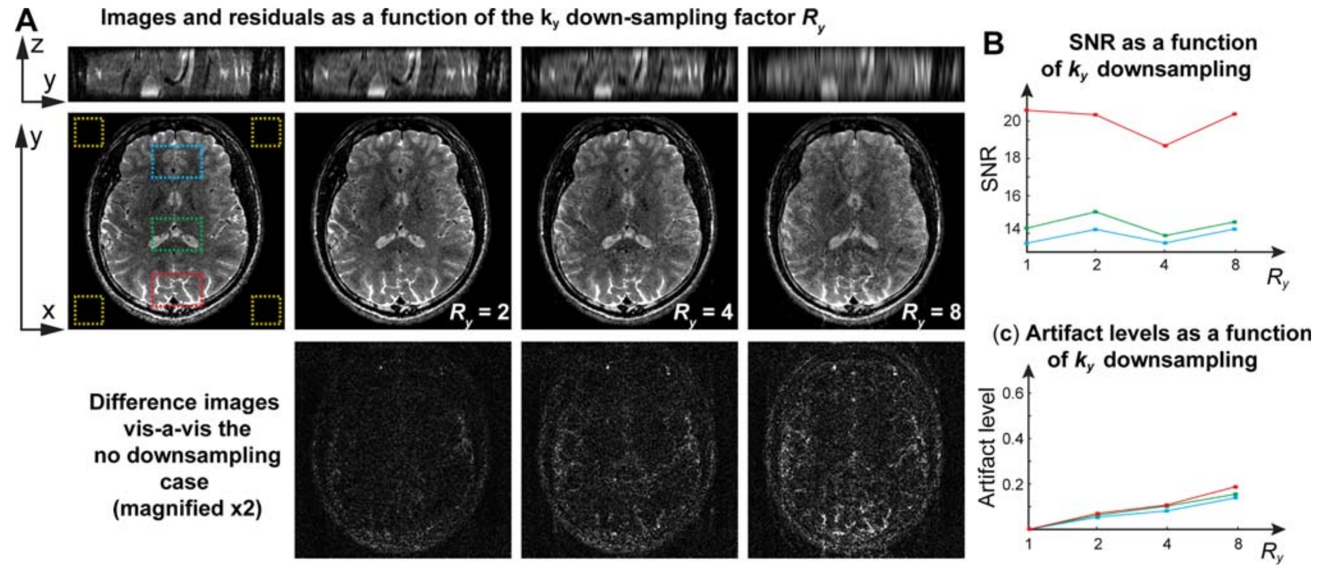

FIGURE 8 Results arising on downsampling the phase-encoded axis of an xSPEN acquisition. (A) Images in the *y-z* and *x-y* planes, including residuals arising on implementing xSPEN MRI with different k_y downsampling factors. The latter are shown as differences (magnified × 2) arising on subtracting each of the latter from the fully sampled reference. (B) SNRs arising from the blue/green/red squares indicated on the leftmost image, calculated by dividing these signals by the noise's SD arising from the yellow squares for in-plane images arising with different downsampling factors. (C) Artifact levels evaluated by taking the ratios between the signals in the various difference images, and the signals arising in the fully sampled image, focusing again on the blue/green/red squares

the imaging gradients used involved $b_{xSPEN} \approx 120$ s/mm^2 values and thereby lead to ≈25% signal attenuations beyond the T_2 losses.

A remarkable aspect stressed in Fig. 2b for multi-scan xSPEN MRI, was its ability to deal with k_y- downsamplings. The folding that this will incur along the *y* axis can be undone by the available low-resolution $y' = k_z/C$ profile—at the expense of resolution along the *z* axis and of eventually increasing artifacts. Figure 8 demonstrates this feature by comparing fully k_y-sampled results with images arising from downsampled experiments. As can be appreciated from the *y-z* plane images, only a substantial downsampling of k_y brings about strong effects in the resolution along *z*—that initially is mostly affected by a reduction in the number of image points. To better gauge these downsampling effects, Figure 8 also focuses on how SNR and artifacts affect images in the *x-y* plane for the same *z*-resolved center slice. At first glance, all these in-plane images look similar, and artificial structures are only visible when the downsampling reaches $R_y = 8$. SNR estimations arising from different regions in the image also lack a clear trend as a function of R_y (Figure 8B), even if artifact levels evaluated by taking differences against the images arising from a fully sampled experiment do evidence a monotonic increase with downsampling (Figure 8C). The artifacts arising in these *x-y* images are dependent on the *z*-axis features for the various *y*-positions and, in this instance, show no particularly evident structure.

Figure 9 demonstrates another feature of multi-scan xSPEN MRI: its built-in ability to zoom into the phase-encoded FOV_y, without suffering from major folding. Indeed, as was the case with its single-shot counterpart,[12] the range of the latter FOV will also be dominated by the encoding chirped pulses. As discussed in connection to Figure 4, however, edge effects that were absent in the single-shot counterparts will arise in the multi-scan phase encoding case. These effects are examined in Figure 9 for slices centered on the back of the brain (position 1) and on the cerebellum (position 2). Whereas no artifacts arise on targeting a full $FOV_y = 192$ mm (Figure 9), zooming to a half $FOV_y = 96$ mm (yellow-dotted regions in Figure 9) shows the onset of aliasing effects. These are not as severe as those often seen in conventional phase encoding methods and involve 2 small edge regions extending over $L_{phase}/2 \approx 2$mm.

4 | DISCUSSION

The present study explored basic features that arise when extending single-shot xSPEN to multi-scan acquisitions. Main rationales for implementing this extension included enhancing the resolution limitations exhibited in all axes by the single-shot technique, making up for the sensitivity losses of the original non-Fourier method, and at the same time seeking to exploit the resilience that single-shot xSPEN showed to field and shift heterogeneities. A solution capable of achieving these aims was devised by adding a phase-encoding loop to the original implementation. Owing to the pre-acquisition hyperbolic phase encoding of the spins, this multi-scan xSPEN variant ended up exhibiting a dual-axis

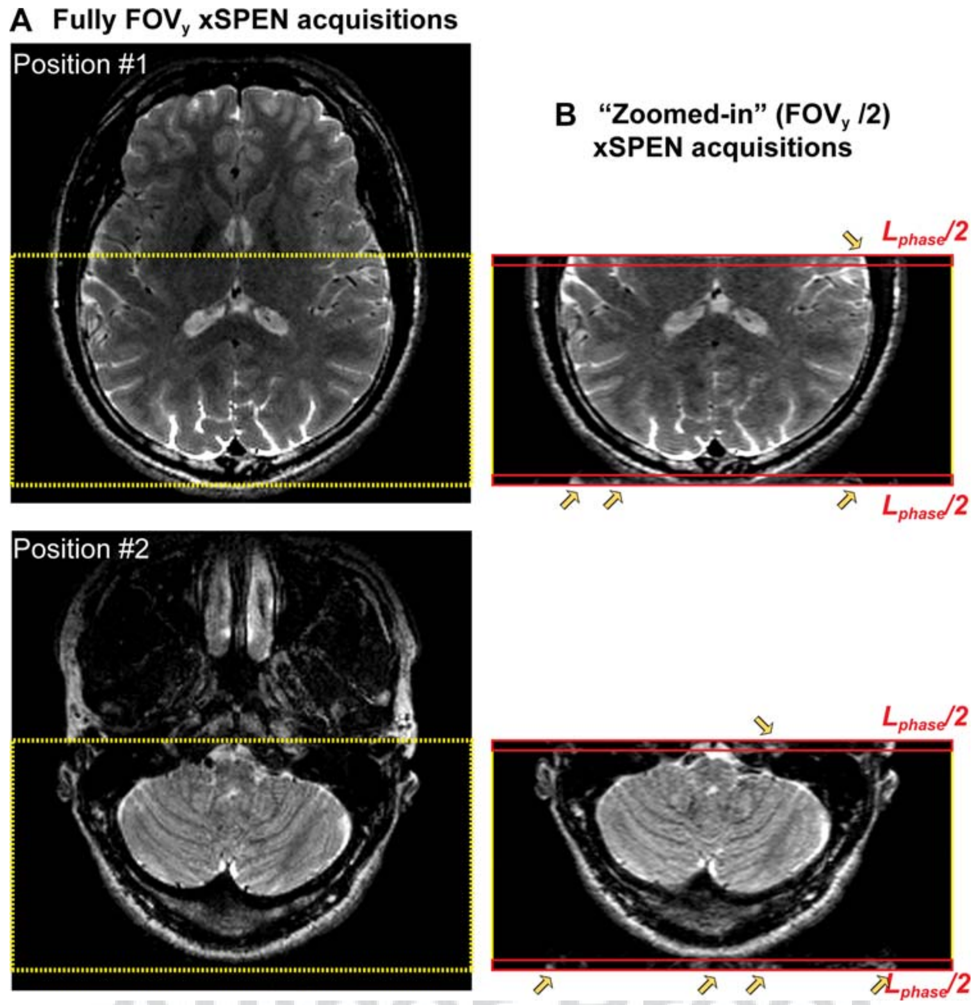

FIGURE 9 Restricted FOV imaging in multi-scan xSPEN MRI. (A) Reference images arising from a full FOV_y (192 mm) xSPEN acquisition. (B) “Zoomed-in” images arising on halving FOV_y to 96 mm (selected yellow dot colored regions in A) exemplifying the folding phenomena introduced in Figure 4. Red rectangles mark the $L_{phase}/2$ regions, exhibiting minor foldovers marked by the yellow arrows

redundancy whereby k_z/k_y not only encoded the imaging information in reciprocal space but also provided low-resolution y/z images in direct spatial space. The first of these features endowed the resulting experiment with resolution and sensitivity without relinquishing on xSPEN's fully refocused acquisition nature, while fully sampling a 3D *k*-space using a single PE loop. At the same time, the redundant information makes the experiment tolerant to downsampling along the PE axis and hence to further acquisition speed ups. In conventional MRI, such downsampling leads to image aliasing, requiring multiple receivers for its unfolding. Folding will also occur in xSPEN, yet this can be undone thanks to redundant information along the k_z/y' axis. PE downsampling may still incur losses of resolution along the SS axis; as explained above, these losses will depend on the degree of features present in the selected slab. Interestingly, it appears that parallel imaging procedures can also be introduced independently from the unfolding considerations above to further accelerate phase-encoded xSPEN MRI scans. A full characterization of this behavior is under investigation.

In terms of SNR/unit_time, multi-scan xSPEN performs most competitively against TSE counterparts when seeking sub-mm 3D spatial resolutions. In the specific cases presented here, we scanned the z axis by interleaving the acquisition of multiple slabs, each with a 12-mm thickness. This choice of slab thickness L_z was somewhat arbitrary and arose as a trade-off between the resolution and SNR being sought, the number of readout echo trains, and the tolerable immunity to field inhomogeneity along the z axis. Indeed, it follows from our theoretical derivations that xSPEN's resolution along the z axis will be given by $\Delta z = L_z/Q$, where Q is both the time-bandwidth product of the encoding pulses as well as the number of elements defining resolution along z. Q generally needs to be $\geq$15 to keep the adiabaticity conditions underlying the frequency-swept-pulse assumption; on the other hand, Q cannot be too large because this is also the number of RO echoes and increasing it excessively will end up in long echo trains and diminished sensitivities. Δz resolution can also be manipulated by changing the L_z slab thickness, yet this is also constrained: very thin slabs will require increased G_z gradients associated to signal losses because of diffusion,[12] whereas thicker slabs will achieve a more efficient coverage of FOV_z yet be subject to distortions caused by field inhomogeneity acting over the course of the slice-selective excitation (that is not subject to xSPEN's full refocusing). In summary, there is a range of L_z , TE, and Q combinations that can lead to similar coverage and resolution characteristics but may have its optimal setting depending also on sensitivity and on the artifact levels that can be tolerated. Supporting Information 2 presents a range of choices that, by themselves or in combination with denoising algorithms, worked well in a variety of brain scans with voxel sizes in the 0.6–1 mm^3 range.

In terms of their data acquisition modules, the main difference between xSPEN and TSE acquisitions is the fact that the former uses a gradient-echo train whereas the latter uses spin-echoes. Normally the T_2^* and field heterogeneity effects in these 2 kinds of echo trains would be dramatically different; xSPEN's in-plane refocusing, however, manages to keep its acquisitions distortion-free without using RF. This, in turn, enables the use of much shorter echo spacings: in the above-mentioned examples these times were 1.03 for xSPEN versus 9.88/13.2 ms for 2D/3D TSE, with the latter 2 delays defined by the selective RF pulses, PE gradient rewinders, and crusher gradients. These shorter acquisition times free xSPEN of blurring phenomena like those arising in TSE because of T_2-related effects (see Supporting Figure S1 for an examples of this).[34] Interestingly, T_2-related effects affecting the signal intensity along the k_z axis may also influence the xSPEN images in the form of a spatially progressive weighting along the orthogonal y-axis. Not relying on RF pulse trains also endowed multi-scan xSPEN with ~50% lower SARs than 3D PE TSE counterparts; this enabled PE xSPEN acquisitions to use ~50% the TRs needed by 3D TSE experiments targeting similar numbers of slabs and of phase-encoding steps, leading to shorter overall volumetric acquisitions. (As for the 2D TSE scans: these should in principle have taken a shorter duration than their 3D TSE counterparts; yet to achieve the high SS definition sought while fulfilling whole brain coverage, a large number of slices had to be collected, leading again to long volumetric scan times). A final consequence arising from xSPEN's RF-free acquisitions is their lack of "bright fat" artifacts,[31] associated in spin echo trains to RF-driven spin-locking effects. Further comparisons on the contrast-to-noise ratios characterizing TSE and xSPEN scans in brain are discussed and illustrated in Supporting Information 3.

Another important acquisition difference arises from xSPEN's demand for a G_z acquisition gradient acting throughout its course. This results in a relatively high diffusion-related *b*-weighting, which makes this 3D imaging technique ~25% less sensitive than comparable 3D TSE counterparts on a per-scan basis. The *z*-axis imaging that this constant gradient makes over the course of the echo planar train also demands that the slab-selection bandwidth be made equal to the inverse of the echo train spacing (i.e., to Δk_z). This requirement is absent in TSE, and for long RO trains it could introduce water–fat displacement problems along the SS dimension; although not used here, fat suppression and/or partial FT_{RO} procedures can alleviate this limitation.

A final property worth noting is xSPEN's zooming capabilities, because restricting FOVs is often a simple means to increase resolution without acquisition time overheads. In conventional phase-encoded MRI, this generally requires saturation filtering bands that increase both the minimum TR as well as the SAR. Multi-scan xSPEN MRI, by contrast, has a built-in restricted FOV capability thanks to the action of frequency-swept encoding pulses along the PE domain (Figure 9). Because of the differences arising between the imaging FOVs targeted by the k_y PE variable and the k_z/y' reading out the SS axis, edge effects arise on zooming that were absent in single-shot counterparts (Figure 4). These spatial compromises, however, are quite small, and could open interesting high-definition applications for imaging small, soft tissues organs.

5 | CONCLUSIONS

This study summarized the main features arising when the robustness of single-shot 2D xSPEN are coupled with the additional sensitivity and resolution arising from phase-encoded multi-scanning. From a fundamental standpoint, it is interesting to notice the similarities and differences that, owing to the hyperbolic phase encoding and xSPEN's special spatiotemporal refocusing conditions, arise between the ensuing experiment and 3D *k*-based MRI alternatives such as TSE. Whereas the latter were implemented without certain improvements that still need to be worked out for xSPEN counterparts—including partial FT, parallel imaging, and multi-band excitation—it was encouraging to see that in crucial parameters including sensitivity per unit time for a given FOV and resolution, the new method compared well with existing alternatives. Furthermore, the xSPEN sequence exhibits a number of features that could open yet additional opportunities. Each step in the phase-encoded procedure, for instance, entails a single-shot xSPEN acquisition providing a low-resolution 2D image; this could enable the scan-by-scan identification and elimination of motional artifacts, leading to very high definition 3D MRI capabilities. Another promise arises from the relatively short acquisition times involved in the xSPEN gradient echo train, which make it compatible with additional spin-echo combinations. These and other potential improvements of the experiments introduced here are currently under investigation.

ACKNOWLEDGMENTS

We are grateful to Dr. Sagit Shushan (Wolfson Medical Center) and the Weizmann MRI team (Edna Furman-Haran, Fanny Attar, and Nachum Stern) for assistance in the human scans. Z.Z. thanks Israel's Council of Higher Education and to the Koshland Foundation for partial postdoctoral fellowships. M.L. acknowledges the Weizmann Institute for a Visiting Faculty Program Fellowship. Financial support from the Israel Science Foundation (795/13), the EU through ERC-2016-PoC (751106), Minerva funding (712277) from the Federal German Ministry for Education and Research, the Kimmel Institute for Magnetic Resonance, and the generosity of the Perlman Family Foundation are also acknowledged.

REFERENCES

[1] Chavhan GB, Babyn PS, Jankharia BG, Cheng HLM, Shroff MM. Steady-state MR imaging sequences: physics, classification, and clinical applications. *Radiographics.* 2008;28:1147-1160.

[2] Oshio K, Jolesz FA, Melki PS, Mulkern RV. T2-weighted thin-section imaging with the multislab three-dimensional RARE technique. *J Magn Reson Imaging.* 1991;1:695-700.

[3] Yuan C, Schmiedl UP, Weinberger E, Krueck WR, Rand SD. Three-dimensional fast spin-echo imaging: pulse sequence and in vivo image evaluation. *J Magn Reson Imaging.* 1993;3:894-899.

[4] Mugler JP. Optimized three-dimensional fast-spin-echo MRI. *J Magn Reson Imaging.* 2014;39:745-767.

[5] Mansfield P. Multi-planar image-formation using NMR spin echoes. *J Phys C.* 1977;10:L55-L58.

[6] Lutti A, Thomas DL, Hutton C, Weiskopf N. High-resolution functional MRI at 3 T: 3D/2D echo-planar imaging with optimized physiological noise correction. *Magn Reson Med.* 2013;69:1657-1664.

[7] Shrot Y, Frydman L. Spatially encoded NMR and the acquisition of 2D magnetic resonance images within a single scan. *J Magn Reson.* 2005;172:179-190.

[8] Tal A, Frydman L. Spatial encoding and the single-scan acquisition of high definition MR images in inhomogeneous fields. *J Magn Reson.* 2006;182:179-194.

[9] Schmidt R, Frydman L. New spatiotemporal approaches for fully refocused, multislice ultrafast 2D MRI. *Magn Reson Med.* 2014; 71:711-722.

[10] Chamberlain R, Park JY, Corum C, et al. RASER: a new ultrafast magnetic resonance imaging method. *Magn Reson Med.* 2007;58:794-799.

[11] Cai C, Dong J, Cai S, et al. An efficient de-convolution reconstruction method for spatiotemporal-encoding single-scan 2D MRI. *J Magn Reson.* 2013;228:136-147.

[12] Zhang Z, Seginer A, Frydman L. Single-scan MRI with exceptional resilience to field heterogeneities. *Magn Reson Med.* 2017; 77:623-634.

[13] Tal A, Frydman L. Single-scan multidimensional magnetic resonance. *Prog Nucl Magn Reson Spectrosc.* 2010;57:241-292.

[14] Paquin R, Pelupessy P, Bodenhausen G. Cross-encoded magnetic resonance imaging in inhomogeneous fields. *J Magn Reson.* 2009;201:199-204.

[15] Solomon E, Liberman G, Zhang Z, Frydman L. Diffusion MRI measurements in challenging head and brain regions via cross-term spatiotemporally encoding. *Sci Rep.* 2017;7: 18010.

[16] Bernstein MA, King KF, Zhou XJ. *Handbook of MRI pulse sequences*. Amsterdam: Academic Press; 2004. 1040 p.

[17] Narsude M, Gallichan D, van der Zwaag W, Gruetter R, Marques JP. Three-dimensional echo planar imaging with controlled aliasing: a sequence for high temporal resolution functional MRI. *Magn Reson Med.* 2016;75:2350-2361.

[18] Ben-Eliezer N, Shrot Y, Frydman L. High-definition, single-scan 2D MRI in inhomogeneous fields using spatial encoding methods. *Magn Reson Imaging.* 2010;28:77-86.

[19] Chen Y, Li J, Qu X, Chen L, et al. Partial Fourier transform reconstruction for single-shot MRI with linear frequency-swept excitation. *Magn Reson Med.* 2013;69:1326-1336.

[20] Chen L, Bao L, Li J, Cai S, Cai C, Chen Z. An aliasing artifacts reducing approach with random undersampling for spatiotemporally encoded single-shot MRI. *J Magn Reson.* 2013;237:115-124.

[21] Seginer A, Schmidt R, Leftin A, Solomon E, Frydman L. Referenceless reconstruction of spatiotemporally encoded imaging data: principles and applications to real-time MRI. *Magn Reson Med.* 2014;72:1687-1695.

[22] Chen L, Li J, Zhang M, et al. Super-resolved enhancing and edge deghosting (SEED) for spatiotemporally encoded single-shot MRI. *Med Image Anal.* 2015;23:1-14.

[23] Ben-Eliezer N, Irani M, Frydman L. Super-resolved spatially encoded single-scan 2D MRI. *Magn Reson Med.* 2010;63:1594-1600.

[24] Garwood M, DelaBarre L. The return of the frequency sweep: designing adiabatic pulses for contemporary NMR. *J Magn Reson.* 2001;153:155-177.

[25] Deshmane A, Gulani V, Griswold MA, Seiberlich N. Parallel MR imaging. *J Magn Reson Imaging*. 2012;36:55-72.

[26] Griswold MA, Jakob PM, Heidemann RM, et al. Generalized autocalibrating partially parallel acquisitions (GRAPPA). *Magn Reson Med.* 2002;47:1202-1210.

[27] Uecker M, Lai P, Murphy MJ, et al. ESPIRiT—an eigenvalue approach to autocalibrating parallel MRI: where SENSE meets GRAPPA. *Magn Reson Med.* 2014;71:990-1001.

[28] Pruessmann KP, Weiger M, Scheidegger MB, Boesiger P. SENSE: sensitivity encoding for fast MRI. *Magn Reson Med.* 1999;42:952-962.

[29] Haacke EM, Lindskogj ED, Lin W. A fast, iterative, partial-fourier technique capable of local phase recovery. *J Magn Reson.* 1991;92:126-145.

[30] MacFall JR, Pelc NJ, Vavrek RM. Correction of spatially dependent phase shifts for partial Fourier imaging. *Magn Reson Imaging.* 1988;6:143-155.

[31] Hardy PA, Henkelman RM, Bishop JE, Poon ECS, Plewes DB. Why fat is bright in rare and fast spin-echo imaging. *J Magn Reson Imaging.* 1992;2:533-540.

[32] Dietrich O, Raya JG, Reeder SB, Reiser MF, Schoenberg SO. Measurement of signal-to-noise ratios in MR images: influence of multichannel coils, parallel imaging, and reconstruction filters. *J Magn Reson Imaging.* 2007;26:375-385.

[33] Kellman P. Image reconstruction in SNR units: a general method for SNR measurement. *Magn Reson Med.* 2007;58:211-212.

[34] Tamir JI, Uecker M, Chen W, Lai P, Alley MT, Vasanawala SS, Lustig M. T2 shuffling: Sharp, multicontrast, volumetric fast spin-echo imaging. *Magn Reson Med.* 2017;77:180-195.

[35] Wu W, Koopmans PJ, Frost R, Miller KL. Reducing slab boundary artifacts in three-dimensional multislab diffusion MRI using nonlinear inversion for slab profile encoding (NPEN). *Magn Reson Med.* 2016;76:1183-1195.

[36] Parker DL, Yuan C, Blatter DD. MR angiography by multiple thin slab 3D acquisition. *Magn Reson Med.* 1991;17:434-451.

SUPPORTING INFORMATION

AQ8 Additional Supporting Information may be found in the online version of this article.

FIGURE S1 SNR performance of the phase-encoded xSPEN and TSE acquisitions. (A and B) PE xSPEN images collected using TR = 2 and TR = 4 s, respectively. (C) Multi-slab 3D TSE images. (D) Multi-slice 2D TSE images. Yellow dot marks the ROIs on which SNR was computed, whereas red arrows show the T_2 blurring effects in TSE experiments. Average SNRs are listing on the bottom of each column. Experimental parameters are detailed in Table 1 of the main text.

FIGURE S2 (A) Raw image with a resolution of $1 \times 1 \times 0.5$ (thickness) mm^3 reconstructed from the phase-encoded xSPEN. (B) Denoised counterpart image arising on using the Block-matching and 4D filtering (BM4D) algorithm. Zoomed images from the red dotted regions of (A) and (B) are shown in the middle column.

FIGURE S3 Contrast in PE xSPEN and in 3D TSE acquisitions (A) PE xSPEN result using TR = 2 s and covering 11 slabs. (B) Multi-slab 3D TSE result using TR = 2 s and covering 3 slabs. (C) Multi-slab 3D TSE using TR = 4 s and covering 11 slabs. All slab thicknesses were 12 mm.

FIGURE S4 CNR values calculated between the 2 indicated voxels in each image. CNR was defined as $|mean(\text{tissue1}) - mean(\text{tissue2})|/std(\text{noise})$, where for each image the 2 red boxes represent the tissue1, tissue2 signals whereas the yellow boxes were used for calculating the SD of the noise.

FIGURE S5 Boundary artifacts arising in multiscan xSPEN if not pushing transition areas outside the targeted region of interests (right) and explanation of why using larger G_y gradients and concurrently large RF sweeping bandwidths will alleviate these problematic edge effects without affecting the slab chosen along the z axis

How to cite this article: Zhang Z, Lustig M, Frydman L. Phase-encoded xSPEN: A novel high-resolution volumetric alternative to RARE MRI. *Magn. Reson. Med.* 2018;00:1–15. https://doi.org/10.1002/mrm.27143